Effect of front surface light trapping structures on the PERC solar cell

Jicheng Zhou[1] [ID] · Yong Tan[1] · Wenfeng Liu[2] · Xianwu Cai[2] · Hailong Huang[2] · Yujin Cao[1]

Abstract

Properties of the front textured surface shape and anti-reflection coating have a great impact on the performance of solar cells. In this paper, the simulation model of the minimum unit cell structure is established and validated, which is based on the framework of Silvaco software and basic parameters of the standard pyramid textures single crystalline silicon PERC solar cell. The effect of the front surface light trapping structures on cell performance is discussed. It is found that the slightly concave pyramid-like textures can improve the response for short wavelengths and the short-circuit current density of the cell is increased by 0.3 mA/cm^2, which is improved by 0.80%. In addition, by properly controlling the preparation process of the anti-reflection coating, a gradient-index SiO_xN_y/Si_3N_4 double-layer anti-reflection coating (DLARC) can be formed, which can significantly reduce the reflectivity for short wavelengths. And the short-circuit current density of the cell can be increased by 0.32 mA/cm^2, which is improved by 0.86%. Finally, the optimized slightly concave pyramid-like textures and the SiO_xN_y/Si_3N_4 DLARC can improve the photoelectric conversion efficiency of the PERC solar cell by 0.18% and 0.20%, respectively.

Keywords PERC solar cell · Light trapping · Texturing · Anti-reflection coating · Device simulation

1 Introduction

PERC (Passivated Emitter and Rear Cell) structure was initially developed in 1989 by University of New South Wales in lab scale [1] and later implemented industrially by the Fraunhofer ISE in 2002 with the pilot-line laser fired contact process [2]. Nowadays, PERC technology has become one of the most cost-effective solutions of high-efficiency c-Si solar cells. The advantage of the PERC solar cell is mainly embodied in its low back surface recombination velocity (SRV). As early as 2006, Hoex et al. [3] utilized Al_2O_3 films prepared by low-temperature plasma-assisted atomic layer deposition (PA-ALD) to reduce the effective SRVs of p-type c-Si to 13 cm/s. Later, Institute for Solar Energy Hamelin (ISFH) reduce the back SRVs of low resistivity p-type c-Si PERC cells to less than 10 cm/s with the highly effective back passivation technology of Al_2O_3/SiN_x stacks [4, 5]. With the process of the back side of c-si solar cells being

perfected [6, 7], researchers try to focus back on the front surface of c-si solar cells. In 2011, Baker-Finchby et al. [8] studied the light trapping paths of the pyramid texture by identifying discrete paths of reflection and the fraction of the reflected light that follows each of these paths, finding that a regular array of inverted pyramids just outperforms a random array of upright pyramids. In 2013, Kim et al. [9] combined the experiment with Silvaco simulation to study the effect of the texture pyramids size on the emitter performance and the front contact resistance of c-si solar cells, and found that solar cells perform better when the pyramids are small. In 2014, Australian National University designed and manufactured an Interdigitated Back Contact (IBC) solar cell with an efficiency of 24.4% using SiO_x/SiN_x DLARC, and compared with the single-layer SiN_x ARC, the short-circuit current is increased by 0.4 mA/cm^2 [10]. In 2015, Bashiri et al. [11] constructed a model of inverted pyramid textures single c-Si solar cell and optimized the

cell performance by varying the inverted pyramid height, which was found that 5 μm inverted pyramid height leads to a maximum cell efficiency. In 2017, Fraunhofer IS proposed the concept of skins for silicon solar cell modeling, which greatly improved the integrity and accuracy of solar cell device simulation by multi-scale modeling [12]. In 2018, Lin et al. [13] improved cell efficiency by approximately 1% through optimizing the pillar texturing of HIT cells.

Textures and ARCs are significant components of solar cells. In high efficiency and industry standard designs, pyramid surface textures play the key role of reducing the reflectivity of the cell surface [8]. Generally, a flat surface has 30% reflectivity, but this can be lowered by texturing the surface [9, 14]. If combined textures with ARCs, a better light trapping effect can be obtained. In photovoltaic industry, the ARC generally consists only of a single layer. Although the single layer ARC, such as Si_3N_4, is relatively simple in fabrication, its working bandwidth is limited and its anti-reflection effect is strongly dependent on the incidence-angle [15]. In principle, a multi-layer ARC gives the best optical performance [16]. Therefore, constructing a multi-layer ARC is another way to improve the front surface light trapping effect. In the case of a double-layer ARC, the first coating can be used to provide excellent surface passivation and anti-reflection, while the second coating is used to provide anti-reflection covering a broader range of solar spectrums.

PERC concept is fully independent from the front side, which means any progress on the front side support the effort to improve cell performance with PERC architecture. Therefore, this paper study the effect of front surface structures based on PERC solar cell. In this paper, TCAD modeling and model verification on the standard (111) pyramid textures single c-Si PERC solar cells with the single layer Si_3N_4 ARC are carried out, and then the effect of the texture shape on the front surface light trapping of the cell is explored. Finally, the SiO_xN_y/Si_3N_4 DLARC is constructed based on the standard pyramid textures to study the gain of the cell performance.

2 Device structure and simulation model

The two-dimensional simulation unit structure of the c-Si PERC solar cell is established by using Athena process simulator and Devedit device structure editor of Silvaco Inc., as shown in Fig. 1. Since there is no symmetry between the front contact and the rear local contact array for most PERC solar cells, it is not easy to select an usual geometrically irreducible standard domain [17]. Therefore, in this paper, the front contact and the rear local contact are placed on the central axis of the simulated unit, and
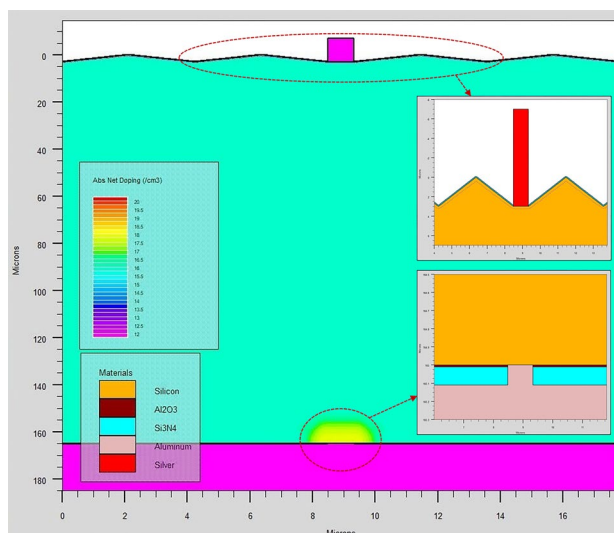

Fig. 1 Two-dimensional simulation unit of c-Si PERC solar cell used in simulation

Table 1 The standard input parameters of the Atlas simulations for model validation

Device parameters	Description	Value
Front textured surface (pyramids)	Angle	54.74°
	Height	3 μm
Bulk property (p type)	Thickness	165 μm
	Doping concentration	6.951×10^{15} cm^{-3}
	SRH lifetime	$\tau_n = 250$ μs $\tau_p = 2500$ μs
Front n + emitter	Surface concentration	1.0×10^{20} cm^{-3}
	Junction depth	~0.4 μm
Front surface passivation	Refractive index	2.00
(Si_3N_4)	Thickness	75 nm
Front contact	Refraction	5%
(Ag)	Height	10 μm
Rear surface passivation	Al_2O_3/Si_3N_4	10 nm/100 nm
LBSF	Surface p+ concentration	1.0×10^{18} cm^{-3}
	Rear junction depth	~12 μm
Rear local contact	Refraction	5%
Rear contact (Al)	Thickness	20 μm

the lateral dimension of the simulated unit is determined according to the front contact shielding fraction and the rear groove fraction. The model is validated with the single c-Si PERC solar cell parameters in Ref. [18], and the specific standard parameters are shown in Table 1. The contact between the electrode and the semiconductor material are ohmic contact. It is assumed that the silicon surface is

an ideal surface. Simulation is implement under the standard test conditions: ambient temperature of 25 °C, AM1.5 spectrum (ASTM G173-03 [19]), spectral irradiance of 100 mW/cm². In ATLAS settings, the light source is at normal incidence. Moreover, the rear internal reflection is considered and the number of reflections is two.

One of the advantages of device simulation is that it can obtain some characteristic parameters of cell that are difficult to measure, such as photo-generation rate, quantum efficiency, etc. ATLAS of Silvaco Inc. predicts the electrical characteristics of physical structures by simulating the transport of carriers through a 2D grid, and it is capable of accurately model a wide range of solar cell operating characteristics [20, 21]. A reliable TCAD simulation is based on the accuracy of the used models. Ray tracing has been regularly used to analyze solar cells. Although it neglects diffraction, ray tracing can account for thill-film optics, textured surfaces and other complex geometries [22]. For relatively thick bulk devices, such as c-Si devices, interference and diffraction effects in the bulk are usually not be concerned about. So ray tracing is useful for planar or textured devices. It is worth mentioning that for textured devices, the texturing must be described explicitly in the device structure when using the Ray tracing method of Silvaco [23]. For textured surfaces, the internal reflection typically requires ray tracing to determine accurately [22]. Setting the refractive index of materials accurately is another crucial part in light propagation model. Optoelectronic device simulation is split into two distinct models that are calculated simultaneously at each DC bias point or transient timestep [23]. Among them, optical ray tracing model use real component of refractive index to calculate the optical intensity at each grid point, while absorption or photogeneration model use the imaginary component of refractive index to calculate a new carrier concentration at each grid point. Since the electrode materials are opaque, the contacts in the model are set to be opaque, namely set the imaginary refractive index of Ag and Al to 1000 to avoid influencing the ray tracing calculations.

The simulation of solar cells can generally be divided into optical and electrical simulation. Good optical design is one of the main approaches for solar cells to achieve high efficiency. It includes reducing the front reflection and enhancing the internal trapping of the cell. The method of optical simulation is to calculate the carrier generation rates in the bulk, and then the three coupled differential equations of the Poisson equation, the electron and hole continuity equations are solved numerically under certain boundary conditions to calculate the electron concentration $n(x)$, the hole concentration $p(x)$, the potential $\phi(x)$ and other internal parameters at the position x in the semiconductor. In this work, Newton iteration method is selected as the numerical calculation

method, and the iterative solution process of the differential equations is completed by Silvaco software. Silvaco ATLAS offers a variety of optional physical models. The concentration-dependent mobility model (conmob), Shockley–Read–Hall recombination model (srh), Auger recombination model (auger), Fermi–Dirac statistic model (fermiairac) and band gap narrowing model (bgn) are chosen as the physical models in the solar cell device simulation process. The Fermi–Dirac statistic model can reduce the carrier concentration in heavily doped regions, which is necessary for high doping($> 10^{18}$ cm^{-3}) [23]. While the band gap narrowing model is one of the most important physical model for semiconductor devices in medium and high doping conditions [24].

The resistivity losses and the recombination losses are two crucial aspects of solar cell power losses. In this model, they were balanced as follows. First, it is considered that the resistivity losses are mainly caused by the bulk resistance, which is related to the doping concentration, and the top lateral resistance, which is determined by the emitter doping concentration, junction depth and mobility. Second, it is considered that the recombination losses are mainly caused by Shockley–Read–Hall recombination and Auger recombination as mentioned before. It is assumed earlier that the silicon surface which covered with the passivation layer is an ideal surface, namely the interface recombination velocity at the silicon surface is set to zero in the model. In other words, this model ignores the surface recombination losses.

Based on the above device structure description, material model description, numerical calculation method selection and model solving process, the results of the characteristic parameters of the cell are shown in Table 2. The simulation results are in the same level with the real cell performance in Ref. [18]. Note that device simulations normally slightly underestimate J_{sc} and slightly overestimate FF, while the simulated V_{oc} is accurate. This leads to relatively accurate final simulation results [18]. The reason for the underestimation of J_{sc} may be that the two-dimensional device simulation overestimates the emitter lateral resistance, while the reason for the overestimation of FF is that the leakage current is neglected in the simulation, namely the shunt resistance is considered to be infinite. The following work will be based on this model. Quantum efficiency,

Table 2 Performance of the PERC solar cell in Ref. [18] and the corresponding Atlas simulation results

	V_{oc} (mV)	J_{sc} (mA/cm²)	FF (%)	η (%)
Ref. [18]	661.3	39.43	79.38	20.69
Atlas	661.1	37.38	83.76	20.69

reflectivity, etc. are important evidence for examining the optical behavior of c-Si solar cells [22], which will subsequently be used to analyze the optical design of the cell. Moreover, for meaningful comparison, identical device parameters were used, although some of them with default value.

In addition, before using the above model for simulation research, in order to further verify the universality of the model, the single c-Si PERC solar cell production data of Hunan Red Solar Photoelectricity Science and Technology CO., LTD. in October 2018 is utilized to conduct a secondary validation. The parameter values in Table 1 are partially replaced according to the process on actual production line, and the corresponding simulation parameters are shown in Table 3. Subsequently, the parameters in Table 3 were used to perform simulation calculations under the same conditions as mentioned before. Finally, the characteristic parameters of the cell are obtained as shown in Table 4. The simulation results are basically consistent with the performance of the PERC solar cell on the actual production line. This also proves once again the accuracy of the device simulation model of the single c-Si PERC solar cell in this paper.

Table 3 The characteristic parameters of the single c-Si PERC solar cell on the actual production line for secondary validation of the model

Device parameters	Description	Value
Front textured surface (pyramids)	Angle	54.74°
	Height	3 μm
Bulk property (p type)	Thickness	180 μm
	Doping concentration	3.272×10^{15} cm^{-3}
	SRH lifetime	$\tau_n = 250$ μs $\tau_p = 2500$ μs
Front n+ emitter	Surface concentration	3.2×10^{20} cm^{-3}
	Junction depth	~0.3 μm
Front surface passivation	Refractive index	2.00
(Si$_3$N$_4$)	Thickness	75 nm
Front contact (Ag)	Refraction	2.3%
	Height	16 μm
Rear surface passivation	Al$_2$O$_3$/Si$_3$N$_4$	10 nm/100 nm
LBSF	Surface p+ concentration	1.0×10^{18} cm^{-3}
	Rear junction depth	~12 μm
Rear local contact	Refraction	5%
Rear contact (Al)	Thickness	20 μm

Table 4 Performance of the PERC solar cell on the actual production line and the corresponding Atlas simulation results

	V_{oc} (mV)	J_{sc} (mA/cm^2)	FF (%)	η (%)
Reference	677.8	39.36	81.95	21.98
Atlas	677.8	38.43	84.29	21.94

3 Effect of texture shapes on cell performance

First, the super-ellipse equation [25] is used to design different texture shapes. Construct the super-ellipse equation as follows:

$$\left(\frac{x}{2.121}\right)^n + \left(\frac{y}{3}\right)^n = 1 \tag{1}$$

where the value range of n is set to 0.2–1.8, and the tolerance is 0.2. Figure 2 shows the corresponding texture shapes in these nine cases, where n = 1 corresponds to the (111) crystal orientation pyramid textures formed by the anisotropic etchant on the (100) crystal orientation c-Si substrate, the angle of the pyramid is 54.74° [26], and the height is 3 μm. It can be seen from the figure that the texture shape is slightly convex pyramid-like structure when 0 < n < 1 and slightly concave pyramid-like structure when 1 < n < 2. At this time, the front surface of (a)–(i) were covered with a Si$_3$N$_4$ ARC with a thickness of 75 nm. Figure 3 shows the short-circuit current density and efficiency of the cells with different texture shapes. It can be seen that cells with the two curved pyramid-like texture shapes, which are closest to the standard pyramid texture shape,
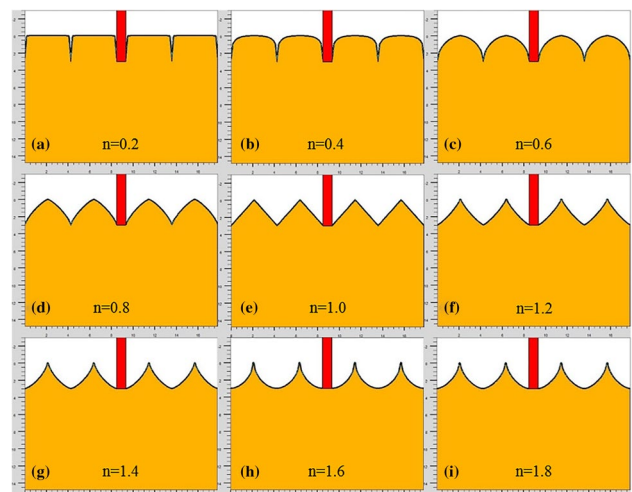
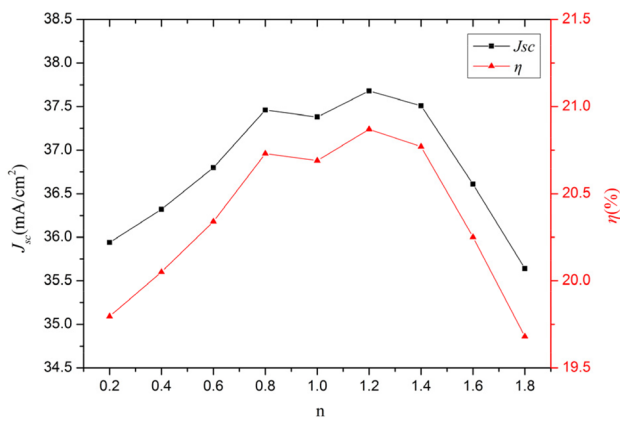**Fig. 2** Surface texture shapes with different values of n for the super-ellipse equation

Fig. 3 Short-circuit current density and efficiency of the cell versus values of n for the super-ellipse equation

can obtain better short-circuit current density and efficiency. And the short-circuit current density and efficiency are 37.68 mA/cm² and 20.87% respectively when n is 1.2, which are increased by 0.3 mA/cm² and 0.18% respectively compared to the reference cell. It is conceivable that the surface area of the slightly concave and slightly convex pyramid-like texture are larger than that of the standard pyramid, so the illumination areas are larger and the light trapping abilities are better.

Figure 4 shows the quantum efficiency of the cells with different texture shapes. As can be seen from the figure, the quantum efficiency of the cell is relatively high in the whole wavelength range when n is 0.8 or 1.2, indicating the spectral response of the cell is good, especially in the short and medium wavelength range of 300–600 nm. In the wavelength range of 600–950 nm, the quantum efficiency of the cells with n of 0.8 and 1.2 are relatively close.
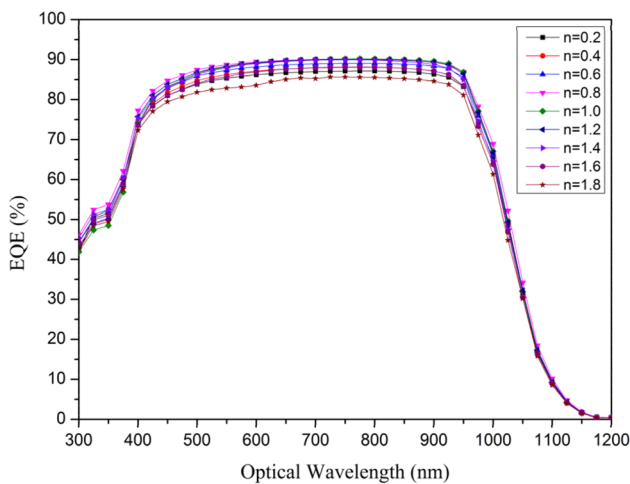
While in the wavelength range of 1000–1200 nm, the overall differences of the quantum efficiency between each case begin to narrow slowly. Since the external quantum efficiency refers to the ratio of the available photocurrent (considering the internal recombination process) to the source photocurrent [23, 27], namely:

$$EQE = \frac{I_{\text{available photocurrent}}}{I_{\text{source photocurrent}}} \tag{2}$$

where the source photocurrent is the amount of current generated by the light source and the available photocurrent is the amount of current absorbed by the semiconductor. In other words, the surface photon reflection losses of the solar cell are not considered. Therefore, the greater the external quantum efficiency, the stronger the light absorption capacity of the cell for the corresponding wavelengths without considering the reflection, also the greater the number of available electron–hole pairs. Meanwhile, it means that the recombination velocity of photogenerated carriers is relatively small. Hence, it can be seen from Fig. 4 that the overall recombination velocity of the cells is comparatively low when n is 0.8 or 1.2. In addition, as the value of n gradually deviates from 1.0, the surface area of the texture increases, and the curvature of texture also increases, resulting in an increase in lattice defects in the emitter region and an increase in recombination, which in turn increases the emitter saturation current. As a result, the performance of the external quantum efficiency is relatively poor when n = 0.2 and 1.8.

Figure 5 shows that reflectivity versus optical wavelength of the cells with different texture shapes. As can be seen from the figure, in the wavelength range of 300–1000 nm, the reflectivity of the cells is both less than 10% when n is 1
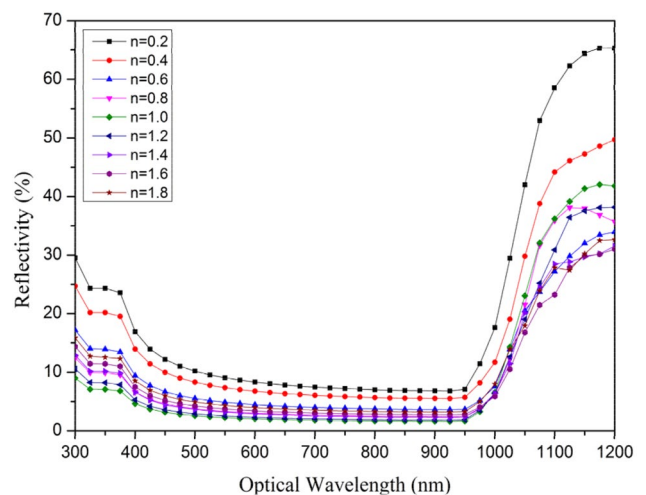

Fig. 4 Quantum efficiency of the cell versus values of n for the super-ellipse equation

Fig. 5 Reflectivity of the cell versus values of n for the super-ellipse equation

or 1.2. In the ultraviolet range, the cell has the lowest reflectivity when n is 1. Meanwhile, noted that in Fig. 4, in the ultraviolet range, the quantum efficiency of the cell is also the lowest when n is taken as 1, indicating that the conventional standard pyramid textures have a lower reflectivity for the ultraviolet range, but the spectral response is relatively poor. In the range of 1000–1200 nm, the reflectivity with n of 1.2 is lower than that with n of 1, indicating that the cell has better light trapping effect on long wavelengths when n is 1.2. In addition to reflectivity and quantum efficiency, the photon flux of the spectrum also affects the performance of the cell [28]. Define the weighted average reflectivity according to Ref. [29]:

$$R_{\mathrm{w}} = \frac{\int_{\lambda_1}^{\lambda_2} F(\lambda) Q_i(\lambda) R(\lambda) d\lambda}{\int_{\lambda_1}^{\lambda_2} F(\lambda) Q_i(\lambda) d\lambda} \qquad (3)$$

where $textF(\lambda)$ is the photon flux at wavelength λ, $Q_i(\lambda)$ is the internal quantum efficiency at wavelength λ, and $R(\lambda)$ is the reflectivity at wavelength λ. The value of $F(\lambda)$ used is extracted from Ref. [29], and $Q(\lambda)$ is given by [29]:

$$Q_i(\lambda) = \frac{Q_e(\lambda)}{1 - R(\lambda)} \qquad (4)$$

where $Q_e(\lambda)$ is the external quantum efficiency of the cell. Finally, the calculated weighted average reflectivity with different values of n is shown in Table 5. The weighted average reflectivity of the cell is 3.50% when n is 1.2, which is almost the same as n of 1. Although the external quantum efficiency of the cell is higher when n is 0.8 as mentioned before, it can be seen from Fig. 5 that the overall reflectivity is higher than n of 1.2, and the calculated weighted average reflectivity is 4.38%. The resulting short-circuit current density and efficiency of the cell are not as high as n of 1.2, which also illustrates the importance of reducing the reflectivity for improving the cell performance.

Figure 6 shows the internal photogeneration rate contours close to the front surface of the cell with different values of n when the beam is at normal incidence. As the figure inset illustrates, due to optical illumination and absorption, the closer to the surface of the cell, the greater the photogeneration rate, and the photogeneration rate gradually decrease with the beam propagation become deeper. In the local area directly beneath the front contact, the corresponding photogeneration rate is low because the light
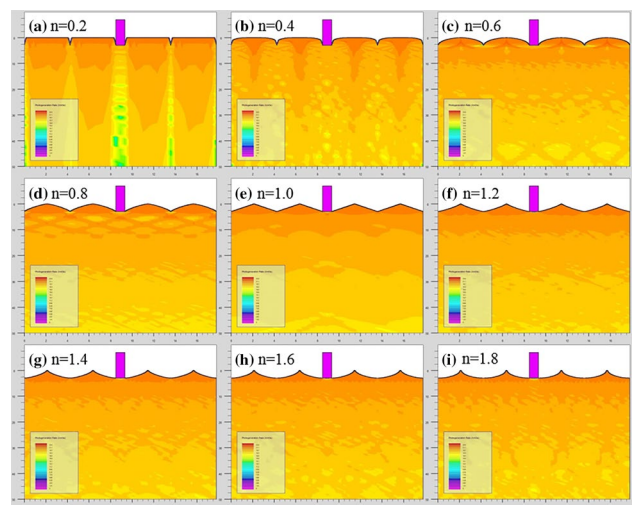

Fig. 6 Photogeneration rate contours of the cell with different values of n for the super-ellipse equation

is difficult to reach there. Meanwhile, the photogeneration rate near the textured surface is large and evenly distributed as shown in Fig. 6d–g, indicating that their light trapping effect are better, which also accounts for the relatively high short-circuit current density and efficiency of the cell when n is 0.8, 1.0, 1.2, and 1.4.

4 Effect of the DLARC on cell performance

In the case of stable incident light intensity, the refractive index and thickness of the ARC are the most important factors determining the effect of the anti-reflection effect. Therefore, it is crucial to match the refractive index and thickness for each of the layers of the DLARC. Currently, the widely used ARC in photovoltaic industry is the silicon nitride coating deposited by PECVD [30]. Note that the deposition of silicon oxynitride can be achieved by simply adding nitrous oxide after inlet silane and ammonia gas during the process of silicon nitride deposition. Moreover, the refractive index of SiO_xN_y varies widely (1.48–1.88), which is convenient for design. Therefore, we choose SiO_xN_y and Si_3N_4 films to finish the design of the DLARC. Generally, materials with relative low refractive index are preferred for the top layer of a DLARC, and higher refractive index materials are usually used for bottom layer materials [31, 32], namely n_1 is generally smaller than n_2. Therefore, Si_3N_4 is chosen as

Table 5 Weighted average reflectivity of different values of n for the super-ellipse equation

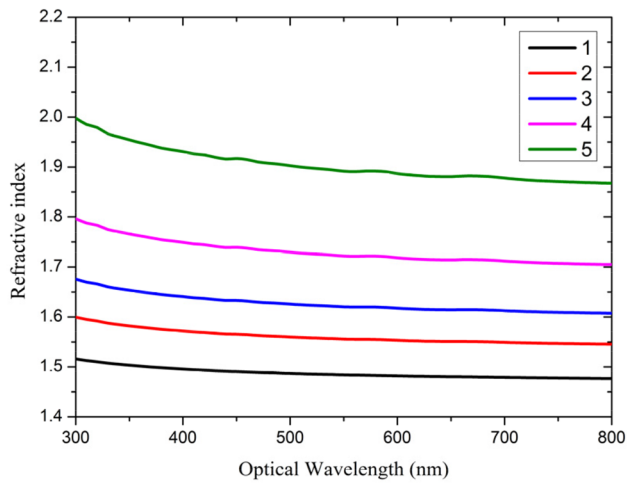| n	0.2	0.4	0.6	0.8	1.0	1.2	1.4	1.6	1.8
R_w (%)	11.50	8.53	5.58	4.38	3.51	3.50	3.97	4.29	5.04

Fig. 7 Refractive index spectrums of SiO$_x$N$_y$ with different nitrogen contents in SOPRA Database

Table 6 Refractive indices of different nitrogen content SiO$_x$N$_y$ at the reference wavelength of 632.8 nm [16] from SOPRA Database

No.	1	2	3	4	5
Nitrogen content (%)	10	20	40	60	80
Refractive index	1.48	1.55	1.62	1.72	1.88

the bottom layer in the simulation, and then the SiO$_x$N$_y$ layer was deposited on the top. The optical data of the Si$_3$N$_4$ and SiO$_x$N$_y$ used in the model are both obtained from SOPRA database. The refractive index of the Si$_3$N$_4$ is around 2.00 at the reference wavelength of 632.8 nm [16], while the refractive index of SiO$_x$N$_y$ is related to its nitrogen content. The optical data for several kinds of SiO$_x$N$_y$ in SOPRA database are shown in Fig. 7 and Table 6. Note that in order to contrast with the reference standard cell model, the subsequent construction and optimization of the DLARC are based on the standard pyramid texture.

Next, the design of the SiO$_x$N$_y$/Si$_3$N$_4$ DLARC is completed by two plans. First, consider applying the single-layer ARC design rule to DLARC circumstances to finish the design of the DLARC (hereinafter referred to as Plan 1). As we known, a quarter wavelength thickness of ARC layer effectively reduces the reflection to minimum at normal incidence. The required optimal single layer thickness for minimum reflection at central wavelength λ is defined by the Eq. 5:

$$d = \frac{\lambda}{4n} \tag{5}$$

where n is the refractive index of the ARC. If it is applied to the DLARC thickness design, then:

Table 7 Optimal thicknesses of different SiO$_x$N$_y$ used in simulation in Plan 1

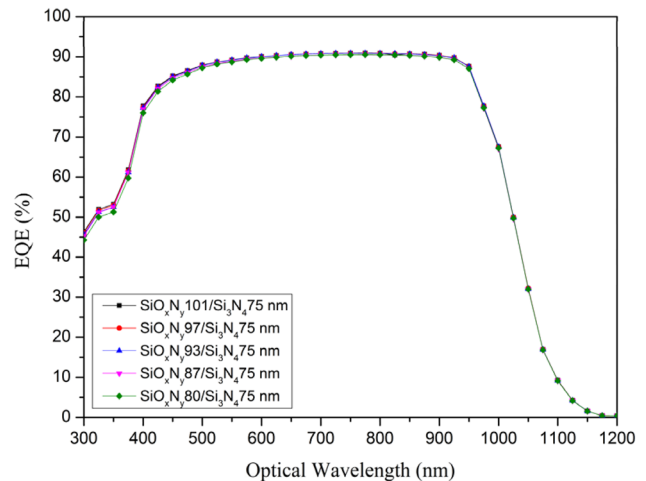| No.	1	2	3	4	5
Refractive index of SiO$_x$N$_y$	1.48	1.55	1.62	1.72	1.88
Refractive index of Si$_3$N$_4$	2.00	2.00	2.00	2.00	2.00
Optimal SiO$_x$N$_y$/Si$_3$N$_4$ DLARC thickness (nm)	101/75	97/75	93/75	87/75	80/75
J_{sc} (mA/cm^2)	37.32	37.39	37.44	37.47	37.48
η (%)	20.67	20.71	20.74	20.76	20.76

Fig. 8 External quantum efficiency of the cell with each SiO$_x$N$_y$/Si$_3$N$_4$ DLARC in Plan 1 versus optical wavelength

$$d_i = \frac{\lambda}{4n_i} \quad (i = 1, 2) \tag{6}$$

where d_1 and d_2 are the optimal thicknesses of the top and bottom layers, respectively. When the central wavelength λ is selected to be 600 nm [33], the optimal thickness of the bottom Si$_3$N$_4$ with a refractive index of 2.00 is 75 nm, which is consistent with the above-mentioned reference standard cell model parameters. On this basis, SiO$_x$N$_y$ with different refractive indices were deposited as the top layer respectively. As a result, five groups of SiO$_x$N$_y$/Si$_3$N$_4$ match schemes were formed. The results are shown in Table 7. It can be seen that when the refractive index gradient between SiO$_x$N$_y$ and Si$_3$N$_4$ layers are small, the short-circuit current density and efficiency of the cell are greatly improved. Figures 8 and 9 show the external quantum efficiency and reflectivity versus optical wavelength of the five groups of schemes respectively. As the figure inset illustrates, the fourth and fifth schemes have relatively poor spectral responses in the ultraviolet range, but their reflectivity for the ultraviolet range is also relatively low. The weighted average reflectivity is calculated to be
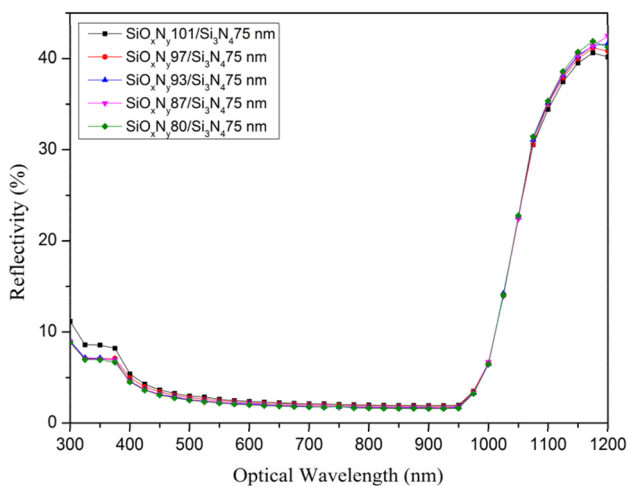
Fig. 9 Reflectivity of the cell with each SiO_xN_y/Si_3N_4 DLARC in Plan 1 versus optical wavelength

Fig. 10 Short-circuit current density of the cell with each SiO_xN_y/Si_3N_4 DLARC in Plan 2

3.49% and 3.44%, respectively. The resulting short-circuit current density and efficiency are inversely higher, which demonstrates again the importance of reducing reflectivity for improving cell performance. In addition, combining Fig. 8 and Table 6, it can be known that as the nitrogen content of the top SiO_xN_y film increases, the overall external quantum efficiency of the cell slightly decreases, which indicates that the recombination of the cell slightly increases, but the overall change is not obvious. The reason may be that the top SiO_xN_y film does not have direct contact with the silicon surface, so it has less effect on the emitter saturation current.

Second, consider adjusting the thickness allocation of the bottom layer and the top layer with fixed total ARC thickness to finish the design of the DLARC (hereinafter referred to as Plan 2). Fix the total ARC thickness of the top SiO_xN_y layer and the bottom Si_3N_4 layer to 75 nm. For each of the above SiO_xN_y with different refractive index in Sopra database, five groups of simulation experiment schemes with different SiO_xN_y/Si_3N_4 thickness allocation (45/30 nm, 50/25 nm, 55/30 nm, 60/15 nm, 65/10 nm) are set. Figures 10 and 11 show the simulation results of the short-circuit current density and efficiency in Plan 2, respectively. On one hand, it can be seen from the figure that the short-circuit current density and efficiency reach the maximum value when the thickness of SiO_xN_y/Si_3N_4 of each group is 60/15 nm. This shows that when the total thickness of the SiO_xN_y/Si_3N_4 DLARC is a constant, there is an optimal Si_3N_4 bottom film thickness of 15 nm, which maximize the cell performance. Figure 12 shows the external quantum efficiency of the cell with each SiO_xN_y/Si_3N_4 DLARC in Plan 2 (both with SiO_xN_y refractive index of 1.88) versus optical wavelength. It can be seen that in the ultraviolet range, the spectral response of the cell is better when the thickness
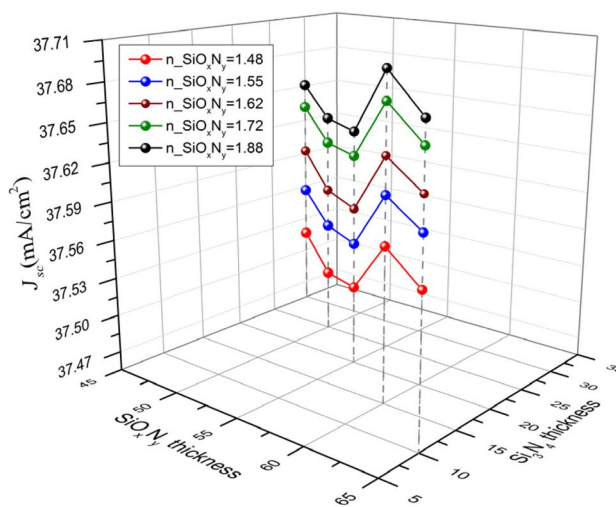
of SiO_xN_y/Si_3N_4 is 60/15 nm, while in the other wavelength range, the spectral response of the five groups are with little difference. This also shows that the reason why the optimal thickness of the Si_3N_4 bottom film is 15 nm is that the SiO_xN_y/Si_3N_4 DLARC has a better spectral response for the ultraviolet band at this time. On the other hand, for different groups, the greater the refractive index of the SiO_xN_y top layer, the better the performance of the cell, which demonstrates again that the smaller the refractive index gradient of the DLARC, the higher the short-circuit current density and efficiency of the cell. Therefore, Fig. 13 shows the reflectivity of the cell with each SiO_xN_y/Si_3N_4 DLARC in Plan 2 (both with SiO_xN_y/Si_3N_4 thicknesses of 60/15 nm) versus optical wavelength. It can be seen that

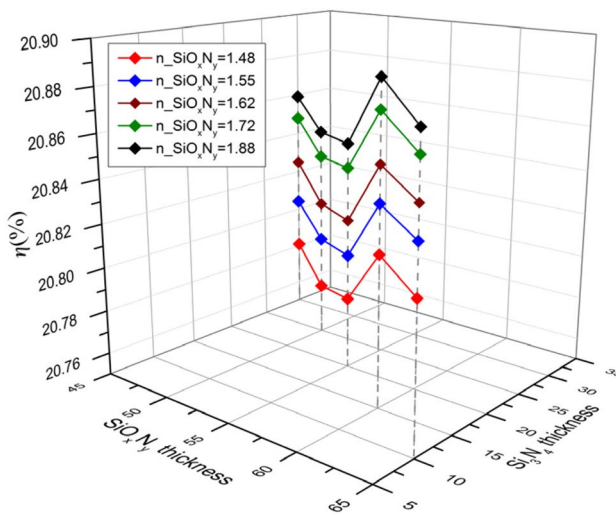**Fig. 11** Efficiency of the cell with each SiO_xN_y/Si_3N_4 DLARC in Plan 2

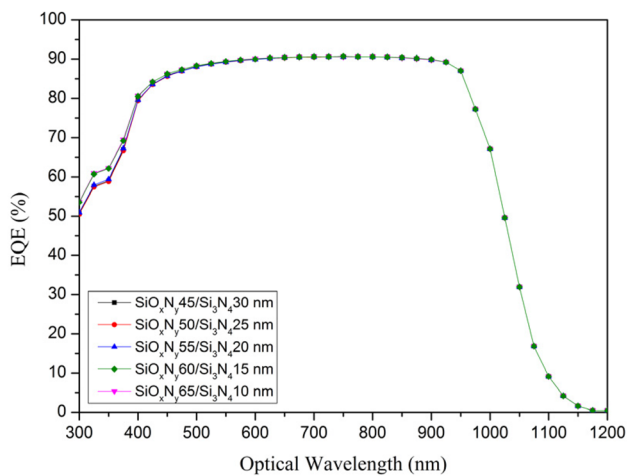**Fig. 12** External quantum efficiency of the cell with each SiO_xN_y/Si_3N_4 DLARC in Plan 2 (both with SiO_xN_y refractive index of 1.88) versus optical wavelength
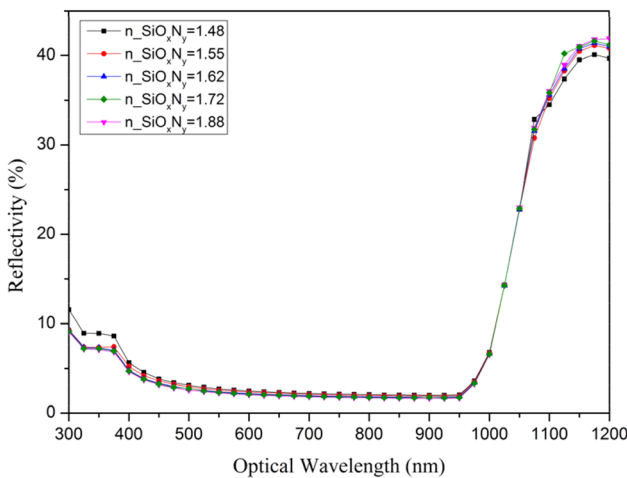

Fig. 13 Reflectivity of the cell with each SiO_xN_y/Si_3N_4 DLARC in Plan 2 (both with SiO_xN_y/Si_3N_4 thicknesses of 60/15 nm) versus optical wavelength

Table 8 Weighted average reflectivity of the cell with different SiO_xN_y refractive index when SiO_xN_y/Si_3N_4 thickness is 60/15 nm

No.	1	2	3	4	5
refractive index of SiO_xN_y	1.48	1.55	1.62	1.72	1.88
R_w (%)	3.94	3.78	3.63	3.58	3.51

in the wavelength range of 300–1000 nm, the higher the refractive index of SiO_xN_y, the lower the reflectivity of the cell. This trend can also be seen from the results of the weighted average reflectivity of each group shown in

Table 8. Hence, the smaller the refractive index gradient of the DLARC, the lower the weighted average reflectivity, and the better the performance of the cell. Combined with the two design plans, it can be found that the SiO_xN_y/Si_3N_4 DLARC has a great influence on the solar radiation in the ultraviolet range, which is mainly determined by the reflectivity characteristics of SiO_xN_y/Si_3N_4 DLARC for short wavelengths. In contrast, Plan 2 shows better results with a short-circuit current density of 37.70 mA/cm^2 and an efficiency of 20.89%. Compared to the reference standard cell, the short-circuit current density is increased by 0.32 mA/cm^2 and the efficiency is increased by 0.20%.

5 Conclusion

(1) A device simulation model, in which the surface recombination is neglected, based on Silvaco Atlas was constructed and validated, which is suitable for exploring the front surface structure characteristics of the single c-Si PERC solar cell.

(2) Compared with the standard pyramid textures, the slightly concave pyramid-like textures can further enhance the light trapping ability of the PERC solar cell due to the larger illumination areas.

(3) The SiO_xN_y/Si_3N_4 DLARC with suitable match of refractive index and thickness can significantly reduce the reflectivity for short wavelengths and consequently improve the short-circuit current density of the cell.

(4) The optimal slightly concave pyramid textures increase the short-circuit current density of the reference standard cell by 0.30 mA/cm^2 and the efficiency by 0.18%. The optimal SiO_xN_y/Si_3N_4 DLARC increases the short-circuit current density of the reference standard cell by 0.32 mA/cm^2 and the efficiency by 0.20%.

Compliance with ethical standards

References

1. Blakers AW, Wang A, Milne AM, Zhao J, Green MA (1989) 22.8% efficient silicon solar cell. Appl Phys Lett 55(13):1363–1365

2. Schneiderlöchner E, Preu R, Lüdemann R, Glunz S (2002) Laser-fired rear contacts for crystalline silicon solar cells. Prog Photovolt Res Appl 10(1):29–34

3. Hoex B, Heil SBS, Langereis E, Van de Sanden MCM, Kessels WMM (2006) Ultralow surface recombination of c-Si substrates passivated by plasma-assisted atomic layer deposited Al_2O_3. Appl Phys Lett 89(4):042112

4. Schmidt J, Veith B, Werner F, Zielke D, Brendel R (2010) Silicon surface passivation by ultrathin Al_2O_3 films and Al_2O_3/SiN_x stacks. In: 35th IEEE photovoltaic specialists conference. IEEE, pp 000885–000890

5. Veith B, Werner F, Zielke D, Brendel R, Schmidt J (2011) Comparison of the thermal stability of single Al_2O_3 layers and Al_2O_3/SiN_x stacks for the surface passiviation of silicon. Energy Procedia 8:307–312

6. Desa MKM, Sapeai S, Azhari AW, Sopian K, Sulaiman MY (2016) Silicon back contact solar cell configuration: a pathway towards higher efficiency. Renew Sustain Energy Rev 60:1516–1532

7. Dullweber T, Schmidt J (2016) Industrial silicon solar cells applying the passivated emitter and rear cell (PERC) concept—a review. IEEE J Photovolt 6(5):1366–1381

8. Baker-Finch SC, McIntosh KR (2011) Reflection of normally incident light from silicon solar cells with pyramidal texture. Prog Photovolt Res Appl 19(4):406–416

9. Kim H, Park S, Kim SM, Kim S, Do Kim Y, Tark SJ, Kim D (2013) Influence of surface texturing conditions on crystalline silicon solar cell performance. Curr Appl Phys 13:S34–S40

10. Franklin E, Fong K, McIntosh K, Fell A, Blakers A, Kho T, Walter D, Wang D, Zin N, Stocks M (2016) Design, fabrication and characterisation of a 24.4% efficient interdigitated back contact solar cell. Prog Photovolt Res Appl 24(4):411–427

11. Bashiri H, Karami AM, Nejad SM (2015) Crystalline silicon solar cell engineering to improve fill factor, open circuit voltage, short circuit current and overall cell efficiency. Modares J Electr Eng 14(4):6–14

12. Fell A, Schön J, Schubert MC, Glunz SW (2017) The concept of skins for silicon solar cell modeling. Sol Energy Mater Sol Cells 173:128–133

13. Lin J-T, Lai C-C, Lee C-T, Hu Y-Y, Ho K-Y, Haga SW (2018) A high-efficiency HIT solar cell with pillar texturing. IEEE J Photovolt 8(3):669–675

14. Ma K, Zeng X, Lei Q, Xue J, Wang Y, Zhao C (2014) Texturization and rounded process of silicon wafers for heterojunction with intrinsic thin-layer solar cells. Frontiers Optoelectron 7(1):46–52

15. Lim KP, Ng DK, Wang Q (2016) Broadband antireflection for a high-index substrate using SiN_x/SiO_2 by inductively coupled plasma chemical vapour deposition. J Phys D Appl Phys 49(8):085302

16. Nagel H, Aberle AG, Hezel R (1999) Optimised antireflection coatings for planar silicon solar cells using remote PECVD silicon nitride and porous silicon dioxide. Prog Photovolt Res Appl 7(4):245–260

17. Altermatt PP (2011) Models for numerical device simulations of crystalline silicon solar cells—a review. J Comput Electron 10(3):314

18. Huang H, Lv J, Bao Y, Xuan R, Sun S, Sneck S, Li S, Modanese C, Savin H, Wang A (2017) 20.8% industrial PERC solar cell: ALD Al_2O_3 rear surface passivation, efficiency loss mechanisms analysis and roadmap to 24%. Sol Energy Mater Sol Cells 161:14–30

19. NREL (2003) Reference air mass 1.5 spectra. https://www.nrel.gov/grid/solar-resource/spectra-am1.5.html. Accessed Jan 2003

20. Michael S, Bates A (2005) The design and optimization of advanced multijunction solar cells using the Silvaco ATLAS software package. Sol Energy Mater Sol Cells 87(1–4):785–794

21. Michael S, Bates A, Green M (2005) Silvaco ATLAS as a solar cell modeling tool. In: Conference record of the thirty-first IEEE photovoltaic specialists conference. IEEE, pp 719-721

22. McIntosh K, Kho T, Fong K, Baker-Finch S, Wan Y, Zin N, Franklin E, Wang D, Abbott M, Grant N (2014) Quantifying the optical losses in back-contact solar cells. In: 2014 IEEE 40th photovoltaic specialist conference (PVSC). IEEE, pp 0115–0123

23. Silvaco Int (2012) ATLAS user's manual device simulation software. Silvaco Int, Santa Clara, pp 558–560

24. Shaker A, Zekry A (2010) A new and simple model for plasma- and doping-induced band gap narrowing. J Electron Devices 8:293–299

25. Shi P-J, Huang J-G, Hui C, Grissino-Mayer HD, Tardif JC, Zhai L-H, Wang F-S, Li B-L (2015) Capturing spiral radial growth of conifers using the superellipse to model tree-ring geometric shape. Frontiers Plant Sci 6:856

26. Zhao J, Green MA (1991) Optimized antireflection coatings for high-efficiency silicon solar cells. IEEE Trans Electron Devices 38(8):1925–1934

27. Chee KW, Tang Z, Lü H, Huang F (2018) Anti-reflective structures for photovoltaics: numerical and experimental design. Energy Rep 4:266–273

28. Bouhafs D, Moussi A, Chikouche A, Ruiz J (1998) Design and simulation of antireflection coating systems for optoelectronic devices: application to silicon solar cells. Sol Energy Mater Sol Cells 52(1–2):79–93

29. Redfield D (1981) Method for evaluation of antireflection coatings. Solar Cells 3(1):27–33

30. Lelièvre JF, Kafle B, Saint-Cast P, Brunet P, Magnan R, Hernandez E, Pouliquen S, Massines F (2019) Efficient silicon nitride SiNx: H antireflective and passivation layers deposited by atmospheric pressure PECVD for silicon solar cells. Prog Photovolt Res Appl 27(11):1007–1019

31. Ko J, Gong D, Pillai K, Lee K-S, Ju M, Choi P, Kim K-R, Yi J, Choi B (2011) Double layer SiN_x: H films for passivation and anti-reflection coating of c-Si solar cells. Thin Solid Films 519(20):6887–6891

32. Lee I, Lim D, Lee S, Yi J (2001) The effects of a double layer anti-reflection coating for a buried contact solar cell application. Surf Coat Technol 137(1):86–91

33. Nagel JR, Scarpulla MA (2010) Enhanced absorption in optically thin solar cells by scattering from embedded dielectric nanoparticles. Opt Express 18(102):A139–A146